Research Article

Nano Research
2021, 14(12): 4650–4657

ISSN 1998-0124 CN 11-5974/O4
https://doi.org/10.1007/s12274-021-3397-9

Elucidating the electro-catalytic oxidation of hydrazine over carbon nanotube-based transition metal single atom catalysts

Jin Zhang[1], Yaxin Wang[1], Chujie Yang[2], Sian Chen[1], Zhengjian Li[1], Yi Cheng[2] (✉), Haining Wang[1] (✉), Yan Xiang[1], Shanfu Lu[1], and Shuangyin Wang[3]

[1] *Beijing Key Laboratory of Bio-inspired Energy Materials and Devices & School of Space and Environment, Beihang University, Beijing 100191, China*
[2] *Department of Environmental Engineering, School of Metallurgy and Environment, Central South University, Changsha 410083, China*
[3] *State Key Laboratory of Chem/Bio-Sensing and Chemometrics, College of Chemistry and Chemical Engineering, Hunan University, Changsha 410082, China*

Received: 11 January 2021 / **Revised:** 8 February 2021 / **Accepted:** 9 February 2021

ABSTRACT

Elucidating the reaction mechanism of hydrazine oxidation reaction (HzOR) over carbon-based catalysts is highly propitious for the rational design of novel electrocatalysts for HzOR. In present work, isolated first-row transition metal atoms have been coordinated with N atoms on the graphite layers of carbon nanotubes via a M-N_4-C configuration (MSA/CNT, M=Fe, Co and Ni). The HzOR over the three single atom catalysts follows a predominant 4-electron reaction pathway to emit N_2 and a negligible 1-electron pathway to emit trace of NH_3, while their electrocatalytic activity for HzOR is dominated by the absorption energy of N_2H_4 on them. Furthermore, FeSA/CNT reverses the passivation effect on Fe/C and shows superior performance than CoSA/CNT and NiSA/CNT with a recorded high mass activity for HzOR due to the higher electronic charge of Fe over Co and Ni in the M-N_4-C configuration and the lowest absorption energy of N_2H_4 on FeSA/CNT among the three MSA/CNT catalysts.

KEYWORDS

hydrazine oxidation, single atom catalyst, transition metals, differential electrochemical mass spectroscopy, direct hydrazine fuel cell

1 Introduction

Polymer electrolyte membrane fuel cell (PEMFC) based on hydrogen has been recognized as one of the most promising solutions to tackle with the surging energy and environmental crisis. However, the challenges on storage and transportation of hydrogen hinder the wide application of PEMFCs. Alternatively, liquid fuels including alcohols, ammonia and hydrazine offer alternatives for the wide spread of PEMFCs [1]. Among them, direct hydrazine fuel cell (DHzFC) thrives with advantages including zero emission of greenhouse gases, high theoretical open circuit voltage (OCV) up to 1.56 V [2] and application of various non-precious catalysts to replace noble metal-based catalysts. In addition, the electrochemical oxidation of hydrazine is also critical for the disposal of this environmental hazard due to its high toxicity and probably carcinogenic.

First-row transition metal catalysts including Co- and Ni-based electrocatalyst have been developed for hydrazine oxidation reaction (HzOR) due to their lower on-set potential than platinum [3]. On the contrary, Fe is seldomly employed as the catalyst for HzOR, since the coverage of an oxidized layer stressed the behavior of Fe electrode for HzOR. So far, great progress have been made on enhancing the electrocatalytic activity of these transition metal catalysts for HzOR by tuning their surface structure and electronic state [4, 5]. However, these electrocatalysts still suffer from agglomeration and corrosion leading to electrocatalytic activity loss in practical DHzFCs operation [6]. Recently, carbon materials [7] and heteroatom-doped carbon materials (N, O and S etc.) have shown considerable electrochemical performance for HzOR by tuning the dopant types as well as density and structures of graphite layers [8]. It has been revealed that the embedment of heteroatoms, especially N atoms modulated the electron environment of adjacent carbon atoms and activated the adsorption of reactants [9]. Nevertheless, the inferior activity of the carbon materials compared to metal catalyst still hinder their application in DHzFC [10].

The emerged carbon supported single-atom catalysts (SACs) or atomically dispersed metal catalysts with embedded metal ions on carbon supports combine the advantages of transition metals and carbon materials [11–15]. In comparison to nano-particles counterpart, SACs show unique electrocatalytic properties due to their high atomic efficiency, unique electronic structure and coordination environment, superior stability and anti-oxidative passivation [16–18]. In addition, the evenly distributed single-atom sites with similar spatial configuration and electronic structure make the SAC isotopically, effectively enhancing the selectivity of catalytic reactions [19]. A number of SACs have been investigated in fuel cell reactions, e.g., formic acid reaction [20] and oxygen reduction reaction [21–25]. However, few attentions were paid for HzOR adopting the SACs. Very recently, selenium SAC (SeNCM) showed superior

Address correspondence to Yi Cheng, yi.cheng@csu.edu.cn; Haining Wang, hwang@buaa.edu.cn

performance than Pt/C for HzOR, paving a pathway for the application of SACs in DHzFC, though the reaction mechanism on it is still unclear [26]. In addition, inspired by the natural hydrazine dehydrogenase enzyme that contains bounded heme C molecule [27] and the great electrochemical performance of earth-abundant SACs in fuel cells, excellent performance of the first-row transition metal SACs for HzOR is expected [28, 29]. Besides, the uniform distribution and well-defined coordination environment of active sites in the SACs offer an ideal platform to investigate the N_2H_4 oxidation mechanism, as the HzOR involves complicated multi-pathways to oxidize the N_2H_4 to H_2 and/or NH_3 [30].

In the present study, atomically dispersed first-row transition metals supported on carbon nanotubes (MSA/CNT, M = Fe, Co and Ni) with a M-N_4-C configuration are explored as electrocatalysts for HzOR. Differential electrochemical mass spectroscopy (DEMS) and density functional theory (DFT) calculation revealed that the HzOR over these SACs follows a predominant 4-electron reaction pathway to emit N_2 and a negligible 1-electron pathway to emit trace of NH_3, while their electrocatalytic activity for HzOR is dominated by the absorption energy of N_2H_4 on them. Due to the highest electronic charge of Fe in the M-N_4-C configuration among the three MSA/CNT catalysts and the lowest absorption energy of N_2H_4 on FeSA/CNT, FeSA/CNT shows superior performance than CoSA/CNT and NiSA/CNT with a recorded high mass activity for HzOR, indicating the promising implementation of first-row transition metal SACs in direct hydrazine fuel cells.

2 Experimental

2.1 Synthesis of MSA/CNT electrocatalysts

The carbon nanotube (0.2 g, < 8 nm in diameter, Nanostructured & Amorphous Materials, USA) was oxidized with HNO_3 (68%, Alfa Aesar) refluxed at 160 °C for 12 h. Then the refluxed CNT (0.1 g) was homogenously mixed with hemin porcine ($C_{34}H_{32}ClFeN_4O_4$, 0.1 g, Sigma-Aldrich) and dicyandiamide ($C_2H_4N_4$, 10 g, Sigma Aldrich) through grinding. The mixture was pyrolyzed sequentially at 350 °C (3 h) and 650 °C (3 h) before being heated at 900 °C for 1 h under argon flow (50 mL·min^{-1}). The as-prepared catalyst was denoted as FeSA/CNT. For Co and Ni single atom catalysts, the cobalt phthalocyanine (CoPc) and nickel phthalocyanine (NiPc) were applied as the metal precursor to replace hemin porcine following the same procedures, and resulted catalysts were denoted as CoSA/CNT and NiSA/CNT. Nitrogen doped CNTs (NCNT) were prepared in the same way without adding metal precursors.

2.2 Characterizations

Transmission electron microscopy (TEM) and high-angle annular dark filed scanning transmission electron microscopy (HAADF-STEM) were carried out on a Titan G2 60-300 at 80 kV. Extended X-ray absorption fine structure (EXAFS) tests were conducted at the wiggler XAS Beamline (12ID) using a set of liquid nitrogen cooled Si(111) monochromator crystals at the Australian Synchrotron in Melbourne, Australia. The exact metal content in the MSA/CNT was conducted by inductively coupled plasma optical emission spectrometer (ICP-OES) via Agilent ICP-OES 730.

Electrocatalytic activity test: 2 mg MSA/CNT catalyst was dispersed in 2 mL Nafion® dispersion with concentration of 0.5 wt.%. The dispersion was treated in an ultrasonic bath for 30 min to obtain a catalyst ink. Then 10 μL of the catalyst ink was deposited into a thin film on a glassy carbon electrode under an infrared lamp for 2 min. The electrocatalytic performance of MSA/CNT for HzOR was tested in a three-electrode cell. A graphite stick electrode and a Hg/HgO electrode filled with 1.0 M KOH were used as a counter electrode and a reference electrode, respectively. The potential of Hg/HgO reference electrode was calibrated by a reversible hydrogen electrode (RHE). The following potential was referred to vs. RHE. The linear scanning voltammetry (LSV) and cyclic voltammetry (CV) measurements were carried out in a 1.0 M KOH solution with N_2 saturated. The accelerated stability test of the MSA/CNT catalysts was conducted in a potential range of 0.2–1.1 V vs. RHE with a scanning rate of 100 mV·s^{-1} for 2,000 cycles. All electrochemical tests were conducted under a CHI 760E potentiostat from Shanghai Chenhua Instrument, China.

DEMS: The DEMS experiments were conducted by a i-DEMS 100 (Shanghai Linglu Instrument Co., Ltd) with a liquid-to-gas interface containing a silicon tube smothered by a Teflon filter membrane. The tubing with vacuum is used to extract gaseous and volatile species from the electrolyte into the spectrometer. During measurements, the liquid-to-gas interface was located above the glassy carbon electrode interface (2 mm distance) in the electrolyte. Argon gas (UHP) with a flow rate of 0.7 mL·min^{-1} was used for monitoring the gaseous or violated species. When the baselines of the mass spectrometer signals were steady, overpotential was employed. The signals were monitored including m/z of 15 and 17 for NH_3, 2 for H_2 and 28 for N_2.

DFT calculation: The DFT calculations were performed with the Vienna *Ab Initio* Simulation Package [31–34]. The calculation details are similar with our previous work [21, 35, 36]. In the calculation, we adopted a catalyst model with Fe, Co or Ni single metal atom and graphene fragment where four C atoms are replaced by N atoms in a supercell of 12.3 × 12.3 × 15.0 Å^3 for all catalyst models [37]. The supercell was large enough to reduce the interaction between metal atoms in adjacent cells. During the calculation, the projector-augmented wave formalism implementing the generalized gradient approximation as parameterized by Perdew et al. [38] was used. The plane-wave kinetic energy cutoff was 400 eV, and the k-points meshes were set as 4 × 4 × 1. All structures were fully relaxed until the convergence in energy and force reached 1.0 × 10^{-4} eV and 1.0 × 10^{-3} eV·Å^{-1}, respectively.

Fuel cell test: The FeSA/CNT catalyst was dispersed into isopropanol with the addition of quaternary ammonia poly (N-methyl-piperidine-*co*-*p*-terphenyl) (QAPPT) ionomer as the binder. The QAPPT was synthesized according to the literature [39]. Then the as-prepared catalyst ink was sprayed into a gas diffusion layer supported by a carbon paper (TGH-G-060, Toray).The catalyst loading for FeSA/CNT is 2.0 mg·cm^{-2} in the anode. The cathode with Pt/C was prepared by the same procedure with a Pt loading 0.5 mg·cm^{-2}. The two electrodes and a QAPPT membrane (50 μm in thickness) were immersed in a 1.0 M KOH solution for 24 h for OH^- exchange. The QAPPT membrane was then sandwiched by the two electrodes via cold-press under 4 MPa for 60 s to form the membrane-electrode-assembly (MEA). The MEA was assembled into a fuel cell hardware with torch force of 4 N·m. The fuel cell was tested by the G20 fuel cell test station, Greenlight Innovation, Canada. The anode was fed by the hydrazine solution with varied flow rate, and the cathode was fed by oxygen with a fixed flow rate of 100 mL·min^{-1}. For a half-cell measurement, the cathode was fed by ultrapure N_2 with a flow rate of 100 mL·min^{-1}, and the anode was fed by the hydrazine solution.

3 Results and discussion

The transition metal SACs were synthesized by pyrolyzing the

blend of CNT and metal precursors under 900 °C and inert atmosphere. The obtained samples maintain the intact structure of CNTs with absent of metal nanoparticles, as indicated by the high resolution TEM in Fig. S1 in the Electronic Supplementary Material (ESM). Furthermore, the aberration corrected HAADF-STEM identifies the individual metal atom supported on the surface of the CNTs, as revealed by the high-density bright dots on CNTs surface (red circles in Fig. 1(a)). In addition, these bright dots have been confirmed as Fe according to the element mapping of FeSA/CNT in Fig. S2 in the ESM, where shows the uniform distribution of Fe and N over the CNTs network. Also, the absence of nanoparticles in the element mapping images and the absence of peaks for metal crystals in XRD patterns (Fig. S3 in the ESM) imply the homogeneous distribution of metal atoms on the surface of the CNTs. Similarly, aberration corrected HAADF-STEM images in Figs. 1(b) and 1(c) indicate the individual dispersion of Co and Ni atoms on CNTs, as convinced by the XPS survey (Fig. S4(a) in the ESM). The inductively coupled plasma optical emission spectroscopy (ICP-OES) confirmed that the exact metal content is 2.8 wt.%, 1.1 wt.% and 4.6 wt.% for FeSA/CNT, CoSA/CNT and NiSA/CNT, respectively [40]. The metal species on the CNTs are identified in the oxidation state by XPS where the XPS high-resolution peak survey of the three samples shows the high content of the Fe^{2+}/Fe^{3+}, Co^{2+} and Ni^{2+} (Figs. S4(b)–S4(d) in the ESM) [41].

The coordination environment of metal atoms supported on CNTs are further investigated by synchrotron X-ray adsorption spectroscopy. Figures 1(d)–1(f) show the bonding environment of MSA/CNT by the Fourier transform EXAFS. There is a peak centered at 1.56 Å in the case of FeSA/CNT (Fig. 1(d)). The features of the peak are very close to that of the FePc with a planar local symmetry of Fe-N_4 configuration in terms of the peak width and peak position [42, 43]. No peak centered at 2.20 Å is observed in the FeSA/CNT, indicating the absence of Fe-Fe bond. Similarly, the peaks centered at 1.53 Å (Fig. 1(e)) and 1.48 Å (Fig. 1(f)) for CoSA/CNT and NiSA/CNT, respectively, are assigned to the Co-N_4 and Ni-N_4 configuration according to the same features as CoPc and NiPc. The absence of Co-Co bond and Ni-Ni bond both centered at 2.18 Å denies the presence of Co and Ni metal particles. These results further confirm that the transition metal SACs are composed of single metal atom with the M-N_4 configuration supported on the CNT surface, as illustrated in Fig. S5 in the ESM.

The practical applications of the transition metal SACs for HzOR has been demonstrated in Fig. 2. The potential of the

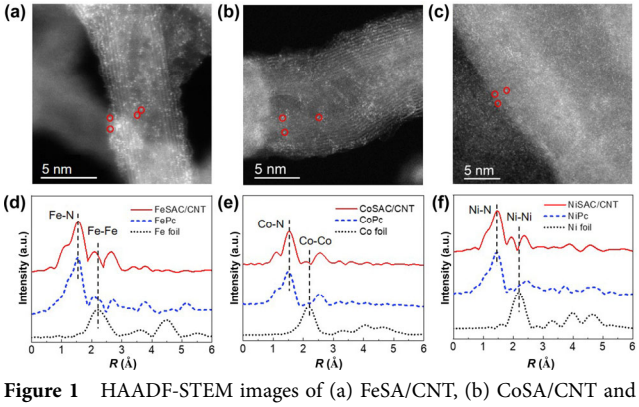

Figure 1 HAADF-STEM images of (a) FeSA/CNT, (b) CoSA/CNT and (c) NiSA/CNT. Some of the single active sites are marked in red circles. (d) Fe K-edge Fourier transformed EXAFS spectra in the R space of FeSA/CNT, FePc and Fe foil, (e) Co K-edge Fourier transformed EXAFS spectra in the *R* space of CoSA/CNT, CoPc and Co foil and (f) Ni K-edge Fourier transformed EXAFS spectra in the *R* space of NiSA/CNT, NiPc and Ni foil.

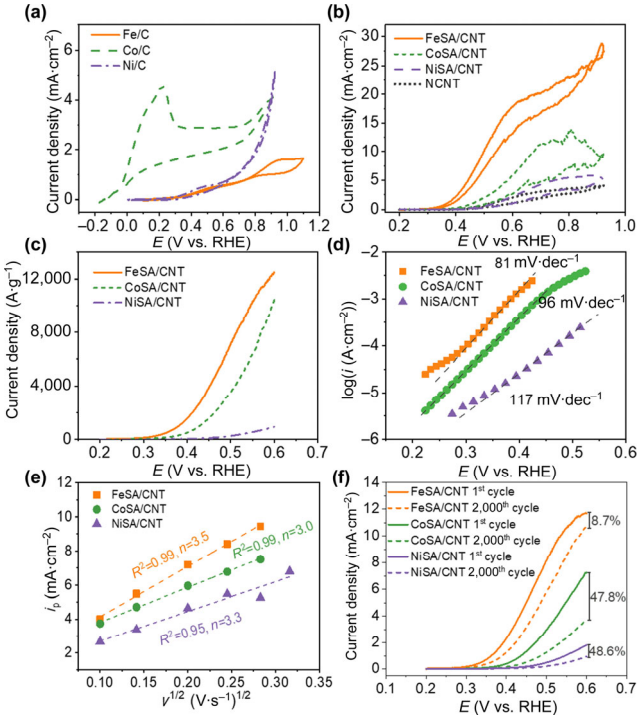

Figure 2 The CV plots of (a) Fe/C, Co/C, Ni/C catalysts and (b) MSA/CNT catalysts and NCNT at N_2 purged 0.1 M N_2H_4 + 1.0 M KOH solution with a scan rate of 5 mV·s^{-1}. (c) The polarization curves of MSA/CNT catalysts normalized by the metal content that was indicated by ICP-OES. (d) Tafel plots of MSA/CNT at N_2 purged 0.1 M N_2H_4 + 1.0 M KOH solution with a scan rate of 5 mV·s^{-1}. (e) Peak current density of MSA/CNT catalysts against the scan rate at N_2 purged 0.01 M N_2H_4 + 1.0 M KOH solution. (f) LSV characterization of MSA/CNT for HzOR before and after the stability test under 0.1 M N_2H_4 + 1.0 M KOH with a scan rate of 5 mV·s^{-1} with a rotating speed of 900 rpm.

reference electrode has been calibrated by a reverse hydrogen electrode (Fig. S6 in the ESM). According to Fig. 2(a), the performance of transition metal nanoparticle catalysts follows the trend of Co/C > Ni/C > Fe/C for HzOR in 0.1 M N_2H_4 + 1.0 M KOH, which is consistent with a literature report by Asazawa et al [44]. However, the current density of Co/C for HzOR is still too low to be used in DHzFC likely due to the passivation effect [45]. When these nanoparticles are transformed into single atoms, the onset potential of FeSA/CNT (0.303 V) for HzOR in 0.1 M N_2H_4 + 1.0 M KOH is 63, 112 and 133 mV negative than that of the CoSA/CNT, NiSA/CNT and NCNT (Fig. 2(b)), respectively. Even in 0.1 M N_2H_4 + 0.1 M KOH, the onset potential of FeSA/CNT (0.338 V) is still much negative than most of the non-precious metal catalysts and carbon-based catalysts (Fig. S7 in the ESM) [26, 27]. Besides, FeSA/CNT shows significantly higher peak current density of 17.2 mA·cm^{-2} under the 0.1 M N_2H_4 + 1.0 M KOH solution with a scan rate of 20 mV·s^{-1} (Fig. S8 in the ESM), which is 5.3 times higher than that of Co/C that shows the best performance among the transition metal nanoparticle catalysts. In addition, the mass activity of FeSA/CNT reaches to 12,493 A·g_{Fe}^{-1} under 0.6 V (Fig. 2(c)), which is significantly higher than that of CoSA/CNT and NiSA/CNT. In addition, it is the best performance among the reported catalysts for HzOR, as listed in Table S1 in the ESM.

To bring an insight on the kinetics of MSA/CNT for HzOR, Tafel plots of these transition metal SACs in 0.1 M N_2H_4 + 1.0 M KOH are recorded in the kinetical-controlled regime of HzOR ranging from 0.27 to 0.42 V (Fig. 2(d)). The Tafel slope of FeSA/CNT, CoSA/CNT and NiSA/CNT is 81, 96 and 111 mV·dec^{-1}, respectively, implying the superior kinetics of FeSA/CNT than

that of CoSA/CNT and NiSA/CNT. Furthermore, FeSA/CNT demonstrates much higher exchange current density (i_0) of 7.4 × 10^{-5} A·cm^{-2} than CoSA/CNT (5.0 × 10^{-5} A·cm^{-2}) and NiSA/CNT (4.5 × 10^{-5} A·cm^{-2}), indicating the superior standard rate constant of FeSA/CNT for HzOR. The linear dependence of the peak current density on $v^{1/2}$ (Fig. S9 in the ESM) indicates the diffusion control process of HzOR on FeSA/CNT, CoSA/CNT and NiSA/CNT, which shows the same behavior as SeNCM and other carbon-based catalysts [26, 46]. Furthermore, the correlations between i_p-$v^{1/2}$ (Fig. 2(e)) and E_p-log$v$ combined the Randles-Sevcik equation reveals the electron transfer number of MSA/CNTs for HzOR [47]. The electron transfer number of FeSA/CNT for HzOR is 3.5, which is higher than the value of 3.0 for CoSA/CNT and 3.3 for NiSA/CNT (Table 1). Their electron transfer number is close to the ideal value (4e$^-$), especially in the case of FeSA/CNT, suggesting reaction pathways of the transition metal SACs for HzOR is mainly through a 4-electron pathway [48].

As stability of catalysts is essential for their practical application in DHzFC, cyclic voltammetry was applied to evaluate their stability under 0.2–0.9 V with a scan rate of 100 mV·s^{-1} for 2,000 cycles in 0.1 M N_2H_4 with 1.0 M KOH. After the durability test, the current density of FeSA/CNT for HzOR under 0.6 V decreases of 8.7%, corresponding to 0.435% per 100 cycles, which is much lower than that of 0.8% per 100 cycles for Se SACs reported [26]. It is also 78.5% and 79.1% lower than the decay rate of CoSA/CNT (2.02% per 100 cycles) and NiSA/CNT (2.08% per 100 cycles) at the same test conditions, respectively (Fig. 2(f)). Besides, the decay rate of MSA/CNT is much lower than their nanoparticle counter parts with decay rate of 3.0% for Ni/C, 2.5% for Co/C and 6.6% for Fe@Cu/C per 100 cycles [49–52], indicating good stability of MSA/CNT during the testing time period.

Although Ni/C and Co/C nanoparticles show much higher electrocatalytic activity than Fe/C nanoparticle [45], FeSA/CNT shows much higher current density and lower onset potential than CoSA/CNT and NiSA/CNT for HzOR at the identical conditions. The results clearly imply the difference of the HzOR mechanism between the transition metal SACs and transition metal nanoparticles [19]. In comparison to the performance of transition metal SACs for HzOR in the solution of 0.01 M N_2H_4 + 1.0 M KOH, the addition of NaSCN that acts as a blocker for the active site of transition metals in the electrolyte causes positive shift of peak potential and onset potential as well as decline of the peak current density (Fig. S10 in the ESM). The results elucidate that M-N_4-C acts as the active site for HzOR, similar to that for oxygen reduction reaction [53]. Consequently, it is reasonable to conclude that the intrinsic activity of the catalysts is determined by the M-N_4-C sites and is in the order of FeSA/CNT> CoSA/ CNT>NiSA/CNT.

On-line differential electrochemical mass spectroscopy has been employed to detect the gaseous products during HzOR by the transition metal SACs, as shown in Fig. 3. Under open circuit potential (OCP), the absent of ionic current density clarifies the absent of gaseous products from HzOR under OCP. With an applied oxidation potential of 0.77 V (Fig. 3(a)),

Table 1 The electrocatalytic activity of MSA/CNT for HzOR under 0.1 M N_2H_4 + 1.0 M KOH with a scan rate of 10 mV·s^{-1}

Samples	Tafel slope (mV·dec^{-1})	i_0 (×10^{-5}) (A·cm^{-2})	Electron transfer number	Reaction order@0.524 V
FeSA/CNT	81	7.4	3.5	0.68
CoSA/CNT	96	5.0	3.0	0.51
NiSA/CNT	117	4.5	3.3	0.41

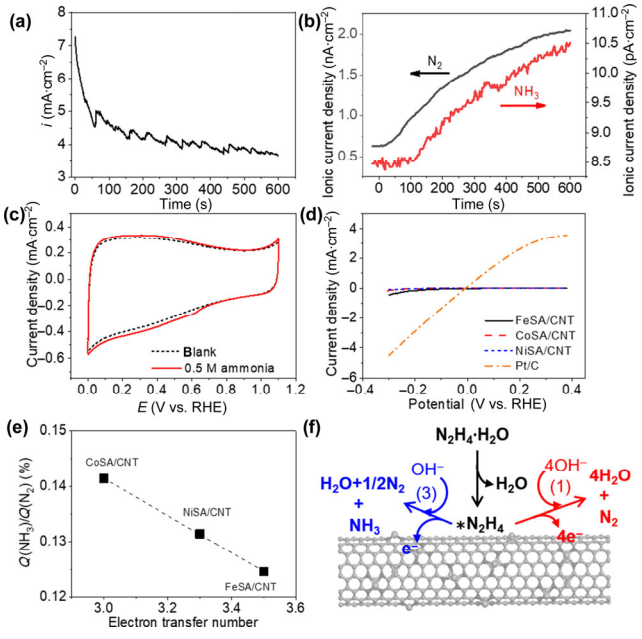

Figure 3 (a) Chronoamperometry curves of FeSA/CNT for HzOR under 0.77 V at 0.1 M N_2H_4 + 1.0 M KOH. DEMS analysis of N_2 (m/z=28) and NH_3(m/z=15) are list in (b). (c) The CV curves of FeSA/CNT on blank and 0.5 M ammonia in 1.0 M KOH. (d) Hydrogen oxidation reaction curves of FeSA/CNT, CoSA/CNT, NiSA/CNT and Pt/C(20 wt.%) in H_2 saturated 1.0 M KOH solution. (e) The ratio of NH_3 charge, $Q(NH_3)$ to N_2 charge, $Q(N_2)$ against the electron transfer number of MSA/CNT for HzOR. (f) Scheme for the two pathways of HzOR by MSA/CNT.

the ionic current density that is assigned to the N_2 (m/z = 28) enhances significantly (Fig. 3(b)). Only trace of NH_3 (ca. 0.5 at.%) has been detected by DEMS during HzOR (Fig. 3(b)). Both the content of N_2 and NH_3 accumulates along with the improvement of applied potential (Fig. S11 in the ESM) or time under a fix potential (Fig. 3(b)). On the contrary, hydrogen is absent under both OCP and applied potentials (Fig. S12 in the ESM). Furthermore, FeSA/CNT shows no activity for the electrochemical oxidation of NH_3 (Fig. 3(c)) and H_2 (Fig. 3(d)). Thus, it is reasonable to conclude that the predominant N_2 and trace of NH_3 are generated during electrochemical oxidation of N_2H_4 instead of chemical decomposition reaction under the ambient atmosphere. Besides FeSA/CNT, dominant N_2 and trace of NH_3 are also detected during HzOR under the applied potential for CoSA/CNT (Fig. S13 in the ESM) and NiSA/CNT (Fig. S14 in the ESM), indicating the similar reaction pathways as FeSA/CNT.

According to Fig. 3(b), the calculated charge ratios of NH_3 to N_2 [$Q(NH_3)/Q(N_2)$] are 0.126%, 0.141% and 0.131% for FeSA/CNT, CoSA/CNT and NiSA/CNT, respectively, which shows reverse correlation with their electron transfer number for HzOR (Fig. 3(e)). In other words, the higher charge ratio of NH_3 to N_2, the lower electron transfer number of the catalyst. That is consistent with the fact that the high performance of the catalyst for HzOR shows low emission of NH_3.

Generally, the oxidation of N_2H_4 in alkaline solutions can be typically through the following pathways (reactions (1)–(5)) to produce H_2 and NH_3 [30]

$$N_2H_4 + 4OH^- \rightarrow N_2 + 4H_2O + 4e^- \quad (1)$$

$$N_2H_4 + xOH^- \rightarrow N_2 + (4–x)/2H_2 + xH_2O + xe^- \quad 1\leq x\leq 3 \quad (2)$$

$$N_2H_4 + OH^- \rightarrow 1/2N_2 + NH_3 + H_2O + e^- \quad (3)$$

$$N_2H_4 \rightarrow N_2 + 2H_2 \quad (4)$$

$$3N_2H_4 \rightarrow N_2 + 4NH_3 \quad (5)$$

For some polycrystalline metal catalysts (e.g., ZrNi alloy [54]),

hydrazine is completely oxidized to nitrogen and water in alkaline media via a 4-electron electrochemical reaction (1) or to N_2 and H_2 via incompletely electrochemical oxidation reaction (2). Besides, the combination of N_2 and H_2 can also be obtained by fully chemical decomposition pathway via reaction (4) (e.g., Pt [55, 56]). In addition, incomplete dehydrogenation of hydrazine via a 1-electron electrochemical oxidation (3) or dissociative reaction (5) tends to generate minor content of NH_3. In this case, the absent of masses m/z 30 (NO), 44 (N_2O) and 46 (NO_2) from the DEMS detection indicate the absent of oxygen intermediate species during HzOR. The absent of H_2 during HzOR excludes the occurrence of reactions (2) and (4), as MSA/CNT catalysts show no activity for hydrogen oxidation reaction [57]. Also, the increased ammonia content along with the applied potential and time under a fix applied potential excludes the chemical decomposition of hydrazine to ammonia via reaction (5). Thereby, the afore-mentioned results indicate that the electrochemical oxidation of hydrazine on FeSA/CNT, CoSA/CNT and NiSA/CNT is mainly through the pathways of reactions (1) with minor extent through reaction (3), which has been proposed in Fig. 3(f).

DFT calculation was further conducted to bring an insight on the superior intrinsic activity of transition metal SACs on HzOR, as shown in Fig. 4. Due to the tiny fraction of NH_3 on the gaseous products, the pathway of electrochemical oxidation of hydrazine to NH_3 with only 1 electron transfer is negligible. In this case, the oxidation pathways of hydrazine on MSA/CNT predominantly follows the consecutive dehydrogenation process as the same as other single atom catalysts [26]. Figure 4(a) shows that hydrazine with sp^3 hybridization possesses gauche conformation on the graphite layer of CNT with the M-N_4-C configuration [58], and there are four intramolecular dehydrogenation steps of HzOR, i.e., $*N_2H_4 \rightarrow *N_2H_3 \rightarrow *N_2H_2 \rightarrow *N_2H \rightarrow *N_2$ [59]. Figure 4(b) shows the interaction energy between the catalyst and each intermediate along the reaction path. Among the three catalysts, FeSA/CNT exhibits the strongest interaction with N_2H_4 (–1.47 eV). The strong interaction could benefit HzOR since the adsorption of the reactant is the first step of the reaction and the stable adsorption of $*N_2H_4$ on the catalyst helps the reaction [60], which is consistent with the highest current density (12,493 $A{\cdot}g_{Fe}^{-1}$) of FeSA/CNT for the HzOR as shown in Fig. 4(c). Meanwhile, there is either uphill or downhill step for the four dehydrogenation reactions on the three catalysts as displayed in Fig. 4(b). According to the Tafel slope value, the transfer coefficient of NiSA/CNT for HzOR is 0.7, while the reaction order of NiSA/CNT derived from the correlation between $\log i_p$ and $\log[N_2H_4]$ [56] is 0.47 under 0.574 V (Fig. S15 in the ESM), implying that the rate determine step of HzOR during the dehydrogenation process is likely the first electron transfer [56, 61]. Consequently, NiSA/CNT holds the largest uphill energy barrier of 1.14 eV for the first step ($*N_2H_4 \rightarrow *N_2H_3$), leading to the lowest catalytic activity NiSA/CNT (Fig. 4(d)). Furthermore, Wang et al. [62–64] fully investigated the modulation of electronic charge of metal atoms at electrocatalytic activities of SACs. The DFT simulation in this case reveals that the charge is 1.05, 0.95 and 0.86 |e| for Fe, Co, and Ni atom of MSA/CNT, respectively. Thereby, the more positive charge of Fe atom in Fe/CNT results in the superior activity for HzOR, which is consistent with the trend of modulation in Wang's work [62–64].

As FeSA/CNT demonstrates the highest electrocatalytic activity towards HzOR among the three transition metal SACs, it has been evaluated in a practical DHzFC. The flow rate of N_2H_4 that feed into the fuel cell has been optimized in a half-cell. The optimum flow rate is 1 $mL{\cdot}min^{-1}$ for the fuel

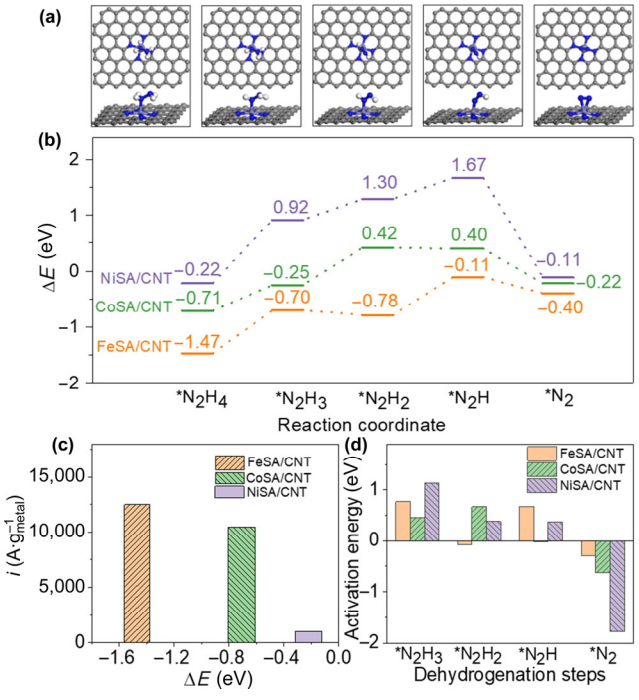

Figure 4 (a) A schematic for the dehydrogenation process of hydrazine on MSA/CNT catalysts. Grey, blue, white, and cyan balls represent C, N, H, and transition metal atoms, respectively. (b) The reaction path of HzOR on different MSA/CNT catalysts. (c) The comparison of the $\Delta E(*N_2H_4)$ and current density at 0.524 V under N_2 purged 0.1 M N_2H_4 + 1.0 M KOH solution with a scan rate of 5 $mV{\cdot}s^{-1}$. (d) The energy barrier of each dehydrogenation step on the MSA/CNT catalysts.

cells (Fig. S16 in the ESM), and further increase of the flow rate will decrease electrocatalytic activity of HzOR in the anode. Figure 5 shows the polarization curves of DHzFC with FeSA/CNT in the anode and Pt/C in the cathode. The open circuit voltage and peak power density of the DHzFC is only 0.76 V and 30.9 $mW{\cdot}cm^{-2}$ at 30 °C, respectively. Increasing the

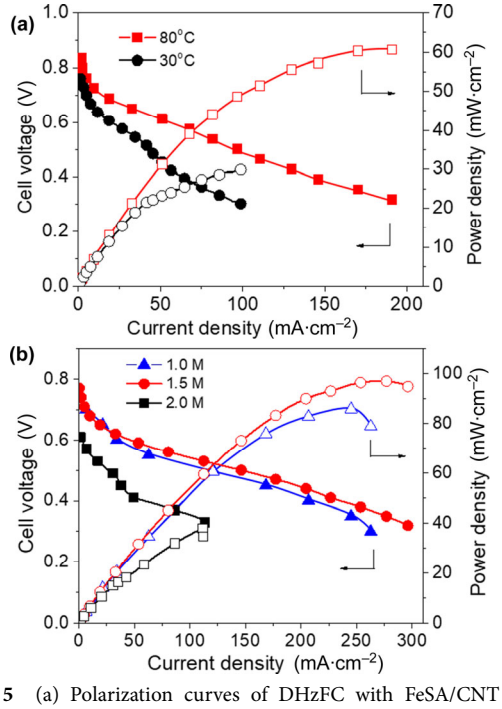

Figure 5 (a) Polarization curves of DHzFC with FeSA/CNT in the anode and Pt/C in the cathode under 30 and 80 °C. The cell was fed by a 0.5 M N_2H_4 solution in the anode and a flow rate of 1.0 $mL{\cdot}min^{-1}$. (b) Polarization curves of DHzFC with different concentration of hydrazine at 80 °C. The flow rate of hydrazine solution in the anode is 1.0 $mL{\cdot}min^{-1}$.

operating temperature significantly increases the OCV and peak power density of the DHzFC to 0.83 V and 60.8 mW·cm^{-2} at 80 °C (Fig. 5(a)), respectively. That is likely due to the increased kinetics of HzOR and the improved ionic conductivity of the polyelectrolyte membrane at high temperature [60]. In addition, the peak power density of DHzFC shows volcano shape along with the increase of the N_2H_4 concentration from 1.0 to 2.0 M and reaches the optimum power density of 97.1 mW·cm^{-2} at 1.5 M N_2H_4. The significantly drop of output power density of the DHzFC at high N_2H_4 concentration is likely due to the server permeation of N_2H_4 [65], which is consistent with the substantial decrease the OCV of DHzFC at high N_2H_4 concentration (Fig. 5(b)) derived from the severe fuel crossover effect. Furthermore, the optimum peak power output is higher than that of DHzFCs based on some metal catalysts in the anode (i.e., Rh/C [55], Pt/C [66] and Zr-Ni alloy [54]) (Table S2 in the ESM). These results demonstrate the potential application of the FeSA/CNT catalyst for DHzFC.

4 Conclusions

The first-row transition metal SACs including Fe, Co and Ni with M-N_4-C active sites show superior electrochemical activity and stability towards HzOR compared to their nanoparticle counterparts. The HzOR over the three SACs follows a predominant 4-electron reaction pathway to emit N_2 and a minor 1-electron pathway to emit trace of NH_3 as elucidated by DEMS. The electrocatalytic activity for HzOR is dominated by the absorption energy of N_2H_4 on them according to the DFT calculation showing a trend of FeSA/CNT > CoSA/CNT > NiSA/CNT. A DHzFC based on FeSA/CNT in the anode achieved a peak power density of 97.1 mW·cm^{-2} under 80 °C, indicating the promising implementation of transition metal SACs in DHzFC.

Acknowledgements

Project supported by Beijing Natural Science Foundation (No. 2194076), the National Natural Science Foundation of China (Nos. 21908001, 21872003, and U19A2017), and the Fundamental Research Funds for the Central Universities. XAS measurements were performed on the soft X-ray and XAS beamlines of the Australian Synchrotron, Victoria, Australia. The electron microscopy carried out at ORNL was supported by the U.S. Department of Energy, Office of Basic Energy Sciences and through a user proposal supported by ORNL's Center for Nanophase Materials Sciences. This research was also supported by the high performance computing (HPC) resources at Beihang University.

Electronic Supplementary Material: Supplementary materials (materials characterizations including TEM, XRD and XPS, electrochemical characterizations including LSV, CV, DEMS and DFT) is available in the online version of this article at https://doi.org/10.1007/s12274-021-3397-9.

References

[1] Zhao, Y.; Setzler, B. P.; Wang, J. H.; Nash, J.; Wang, T.; Xu, B. J.; Yan, Y. S. An efficient direct ammonia fuel cell for affordable carbon-neutral transportation. *Joule* **2019**, *3*, 2472–2484.

[2] Serov, A.; Kwak, C. Direct hydrazine fuel cells: A review. *Appl. Catal. B Environ*. **2010**, *98*, 1–9.

[3] Feng, G.; Kuang, Y.; Li, Y. J.; Sun, X. M. Three-dimensional porous superaerophobic nickel nanoflower electrodes for high-performance hydrazine oxidation. *Nano Res*. **2015**, *8*, 3365–3371.

[4] Du, X. Q.; Liu, C.; Du, C.; Cai, P.; Cheng, G. Z.; Luo, W. Nitrogen-doped graphene hydrogel-supported NiPt-CeO_x nanocomposites and their superior catalysis for hydrogen generation from hydrazine at room temperature. *Nano Res*. **2017**, *10*, 2856–2865.

[5] Xia, B. Q.; Chen, K.; Luo, W.; Cheng, G. Z. NiRh nanoparticles supported on nitrogen-doped porous carbon as highly efficient catalysts for dehydrogenation of hydrazine in alkaline solution. *Nano Res*. **2015**, *8*, 3472–3479.

[6] Burshtein, T. Y.; Farber, E. M.; Ojha, K.; Eisenberg, D. Revealing structure–activity links in hydrazine oxidation: Doping and nanostructure in carbide–carbon electrocatalysts. *J. Mater. Chem. A* **2019**, *7*, 23854–23861.

[7] Zhang, T.; Asefa, T. Heteroatom-doped carbon materials for hydrazine oxidation. *Adv. Mater*. **2019**, *31*, 1804394.

[8] Cazetta, A. L.; Zhang, T.; Silva, T. L.; Almeida, V. C.; Asefa, T. Bone char-derived metal-free N- and S-co-doped nanoporous carbon and its efficient electrocatalytic activity for hydrazine oxidation. *Appl. Catal. B Environ*. **2018**, *225*, 30–39.

[9] Jeong, J.; Choun, M.; Lee, J. Tree-bark-shaped n-doped porous carbon anode for hydrazine fuel cells. *Angew. Chem., Int. Ed*. **2017**, *56*, 13513–13516.

[10] Meng, Y. Y.; Zou, X. X.; Huang, X. X.; Goswami, A.; Liu, Z. W.; Asefa, T. Polypyrrole-derived nitrogen and oxygen Co-doped mesoporous carbons as efficient metal-free electrocatalyst for hydrazine oxidation. *Adv. Mater*. **2014**, *26*, 6510–6516.

[11] Qiao, B. T.; Wang, A. Q.; Yang, X. F.; Allard, L. F.; Jiang, Z.; Cui, Y. T.; Liu, J. Y.; Li, J.; Zhang, T. Single-atom catalysis of CO oxidation using Pt_1/FeO_x. *Nat. Chem*. **2011**, *3*, 634–641.

[12] Cheng, Y.; Zhao, S. Y.; Li, H. B.; He, S.; Veder, J. P.; Johannessen, B.; Xiao, J. P.; Lu, S. F.; Pan, J.; Chisholm, M. F. et al. Unsaturated edge-anchored Ni single atoms on porous microwave exfoliated graphene oxide for electrochemical CO_2. *Appl. Catal. B Environ*. **2019**, *243*, 294–303.

[13] Cheng, Y.; Zhao, S. Y.; Johannessen, B.; Veder, J. P.; Saunders, M.; Rowles, M. R.; Cheng, M.; Liu, C.; Chisholm, M. F.; De Marco, R. et al. Atomically dispersed transition metals on carbon nanotubes with ultrahigh loading for selective electrochemical carbon dioxide reduction. *Adv. Mater*. **2018**, *30*, 1706287.

[14] Wang, Y. C.; Liu, Y.; Liu, W.; Wu, J.; Li, Q.; Feng, Q. G.; Chen, Z. Y.; Xiong, X.; Wang, D. S.; Lei, Y. P. Regulating the coordination structure of metal single atoms for efficient electrocatalytic CO_2 reduction. *Energy Environ. Sci*. **2020**, *13*, 4609–4624.

[15] Chen, Y. J.; Ji, S. F.; Sun, W. M.; Lei, Y. P.; Wang, Q. C.; Li, A.; Chen, W. X.; Zhou, G.; Zhang, Z. D.; Wang, Y. et al. Engineering the atomic interface with single platinum atoms for enhanced photocatalytic hydrogen production. *Angew. Chem., Int. Ed*. **2020**, *59*, 1295–1301.

[16] Li, H.; Zhang, H. X.; Yan, X. L.; Xu, B. S.; Guo, J. J. Carbon-supported metal single atom catalysts. *New Carbon Mater*. **2018**, *33*, 1–11.

[17] Cheng, Y.; He, S.; Lu, S. F.; Veder, J. P.; Johannessen, B.; Thomsen, L.; Saunders, M.; Becker, T.; De Marco, R.; Li, Q. F. et al. Iron single atoms on graphene as nonprecious metal catalysts for high-temperature polymer electrolyte membrane fuel cells. *Adv. Sci*. **2019**, *6*, 1802066.

[18] Zhang, N. Q.; Ye, C. L.; Yan, H.; Li, L. C.; He, H.; Wang, D. S.; Li, Y. D. Single-atom site catalysts for environmental catalysis. *Nano Res*. **2020**, *13*, 3165–3182.

[19] Ou, H. H.; Wang, D. S.; Li, Y. D. How to select effective electrocatalysts: Nano or single atom? *Nano Sel.*, in press. DOI: 10.1002/nano.202000239.

[20] Xiong, Y.; Dong, J. C.; Huang, Z. Q.; Xin, P. Y.; Chen, W. X.; Wang, Y.; Li, Z.; Jin, Z.; Xing, W.; Zhuang, Z. B. et al. Single-atom Rh/N-doped carbon electrocatalyst for formic acid oxidation. *Nat. Nanotechnol*. **2020**, *15*, 390–397.

[21] Cui, L. T.; Cui, L. R.; Li, Z. J.; Zhang, J.; Wang, H. N.; Lu, S. F.; Xiang, Y. A copper single-atom catalyst towards efficient and durable oxygen reduction for fuel cells. *J. Mater. Chem. A* **2019**, *7*, 16690–16695.

[22] Wang, J.; Liu, W.; Luo, G.; Li, Z. J.; Zhao, C.; Zhang, H. R.; Zhu, M. Z.; Xu, Q.; Wang, X. Q.; Zhao, C. M. et al. Synergistic effect of well-defined dual sites boosting the oxygen reduction reaction. *Energy Environ. Sci*. **2018**, *11*, 3375–3379.

[23] Qu, Y. T.; Li, Z. J.; Chen, W. X.; Lin, Y.; Yuan, T. W.; Yang, Z. K.; Zhao, C. M.; Wang, J.; Zhao, C.; Wang, X. et al. Direct transformation of bulk copper into copper single sites via emitting and trapping of atoms. *Nat. Catal.* **2018**, *1*, 781–786.

[24] Cheng, Y.; He, S.; Veder, J. P.; De Marco, R.; Yang, S. Z.; Jiang, S. P. Atomically dispersed bimetallic feni catalysts as highly efficient bifunctional catalysts for reversible oxygen evolution and oxygen reduction reactions. *ChemElectroChem* **2019**, *6*, 3478–3487.

[25] Sun, T. T.; Xu, L. B.; Wang, D. S.; Li, Y. D. Metal organic frameworks derived single atom catalysts for electrocatalytic energy conversion. *Nano Res.* **2019**, *12*, 2067–2080.

[26] Wang, T. Z.; Wang, Q.; Wang, Y. C.; Da, Y. L.; Zhou, W.; Shao, Y.; Li, D. B.; Zhan, S. H.; Yuan, J. Y.; Wang, H. Atomically dispersed semimetallic selenium on porous carbon membrane as an electrode for hydrazine fuel cells. *Angew. Chem., Int. Ed.* **2019**, *58*, 13466–13471.

[27] Ojha, K.; Farber, E. M.; Burshtein, T. Y.; Eisenberg, D. A multi-doped electrocatalyst for efficient hydrazine oxidation. *Angew. Chem., Int. Ed.* **2018**, *57*, 17168–17172.

[28] Wang, J.; Huang, Z. Q.; Liu, W.; Chang, C. R.; Tang, H. L.; Li, Z. J.; Chen, W. X.; Jia, C. J.; Yao, T.; Wei, S. Q. et al. Design of n-coordinated dual-metal sites: A stable and active Pt-free catalyst for acidic oxygen reduction reaction. *J. Am. Chem. Soc.* **2017**, *139*, 17281–17284.

[29] Li, Z. J.; Wang, D. H.; Wu, Y. E.; Li, Y. D. Recent advances in the precise control of isolated single-site catalysts by chemical methods. *Natl. Sci. Rev.* **2018**, *5*, 673–689.

[30] Asazawa, K.; Sakamoto, T.; Yamaguchi, S.; Yamada, K.; Fujikawa, H.; Tanaka, H.; Oguro, K. Study of anode catalysts and fuel concentration on direct hydrazine alkaline anion-exchange membrane fuel cells. *J. Electrochem. Soc.* **2009**, *156*, B509–B512.

[31] Kresse, G.; Hafner, J. *Ab initio* molecular-dynamics simulation of the liquid-metal-amorphous-semiconductor transition in germanium. *Phys. Rev. B* **1994**, *49*, 14251–14269.

[32] Kresse, G.; Furthmüller, J. Efficiency of *ab-initio* total energy calculations for metals and semiconductors using a plane-wave basis set. *Comput. Mater. Sci.* **1996**, *6*, 15–50.

[33] Kresse, G.; Furthmüller, J. Efficient iterative schemes for *ab initio* total-energy calculations using a plane-wave basis set. *Phys. Rev. B* **1996**, *54*, 11169–11186.

[34] Kresse, G.; Hafner, J. *Ab initio* molecular dynamics for liquid metals. *Phys. Rev. B* **1993**, *47*, 558–561.

[35] Cui, L. T.; Li, Z. J.; Wang, H. N.; Cui, L. R.; Zhang, J.; Lu, S. F.; Xiang, Y. Atomically dispersed Cu–N–C as a promising support for low-Pt loading cathode catalysts of fuel cells. *ACS Appl. Energy Mater.* **2020**, *3*, 3807–3814.

[36] Guo, M.; Wang, H. N.; Cui, L. T.; Zhang, J.; Xiang, Y.; Lu, S. F. Nickel promoted palladium nanoparticles for electrocatalysis of carbohydrazide oxidation reaction. *Small* **2019**, *15*, 1900929.

[37] Xu, H. X.; Cheng, D. J.; Cao, D. P.; Zeng, X. C. A universal principle for a rational design of single-atom electrocatalysts. *Nat. Catal.* **2018**, *1*, 339–348.

[38] Perdew, J. P.; Burke, K.; Ernzerhof, M. Generalized gradient approximation made simple. *Phys. Rev. Lett.* **1996**, *77*, 3865–3868.

[39] Peng, H. Q.; Li, Q. H.; Hu, M. X.; Xiao, L.; Lu, J. T.; Zhuang, L. Alkaline polymer electrolyte fuel cells stably working at 80 °C. *J. Power Sources* **2018**, *390*, 165–167.

[40] Xiong, Y.; Sun, W. M.; Han, Y. H.; Xin, P. Y.; Zheng, X. S.; Yan, W. S.; Dong, J. C.; Zhang, J.; Wang, D. S.; Li, Y. D. Cobalt single atom site catalysts with ultrahigh metal loading for enhanced aerobic oxidation of ethylbenzene. *Nano Res.*, in press, DOI: 10.1007/s12274-020-3244-4.

[41] Fu, Y.; Yu, H. Y.; Jiang, C.; Zhang, T. H.; Zhan, R.; Li, X. W.; Li, J. F.; Tian, J. H.; Yang, R. Z. Nico alloy nanoparticles decorated on N-doped carbon nanofibers as highly active and durable oxygen electrocatalyst. *Adv. Funct. Mater.* **2018**, *28*, 1705094.

[42] Li, X. Y.; Rong, H. P.; Zhang, J. T.; Wang, D. S.; Li, Y. D. Modulating the local coordination environment of single-atom catalysts for enhanced catalytic performance. *Nano Res.* **2020**, *13*, 1842–1855.

[43] Zhang, J.; Zheng, C. Y.; Zhang, M. L.; Qiu, Y. J.; Xu, Q.; Cheong, W. C.; Chen, W. X.; Zheng, L. R.; Gu, L.; Hu, Z. P. et al. Controlling N-doping type in carbon to boost single-atom site Cu catalyzed transfer hydrogenation of quinoline. *Nano Res.* **2020**, *13*, 3082–3087.

[44] Asazawa, K.; Yamada, K.; Tanaka, H.; Taniguchi, M.; Oguro, K. Electrochemical oxidation of hydrazine and its derivatives on the surface of metal electrodes in alkaline media. *J. Power Sources* **2009**, *191*, 362–365.

[45] Jeon, T. Y.; Watanabe, M.; Miyatake, K. Carbon segregation-induced highly metallic Ni nanoparticles for electrocatalytic oxidation of hydrazine in alkaline media. *ACS Appl. Mater. Interfaces* **2014**, *6*, 18445–18449.

[46] Fragal, V. H.; Fragal, E. H.; Zhang, T.; Huang, X. X.; Cellet, T. S. P.; Pereira, G. M.; Jitianu, A.; Rubira, A. F.; Silva, R.; Asefa, T. Deriving efficient porous heteroatom-doped carbon electrocatalysts for hydrazine oxidation from transition metal ions-coordinated casein. *Adv. Funct. Mater.* **2019**, *29*, 1808486.

[47] Liu, C. B.; Zhang, H.; Tang, Y. H.; Luo, S. L. Controllable growth of graphene/Cu composite and its nanoarchitecture-dependent electrocatalytic activity to hydrazine oxidation. *J. Mater. Chem. A* **2014**, *2*, 4580–4587.

[48] Sanabria-Chinchilla, J.; Asazawa, K.; Sakamoto, T.; Yamada, K.; Tanaka, H.; Strasser, P. Noble metal-free hydrazine fuel cell catalysts: EPOC effect in competing chemical and electrochemical reaction pathways. *J. Am. Chem. Soc.* **2011**, *133*, 5425–5431.

[49] Wang, H.; Ma, Y. J.; Wang, R. F.; Key, J.; Linkov, V.; Ji, S. Liquid-liquid interface-mediated room-temperature synthesis of amorphous NiCo pompoms from ultrathin nanosheets with high catalytic activity for hydrazine oxidation. *Chem. Commun.* **2015**, *51*, 3570–3573.

[50] Wen, X. P.; Dai, H. B.; Wu, L. S.; Wang, P. Electroless plating of Ni-B film as a binder-free highly efficient electrocatalyst for hydrazine oxidation. *Appl. Surf. Sci.* **2017**, *409*, 132–139.

[51] Wang, Y. H.; Liu, X. Y.; Tan, T.; Ren, Z. L.; Lei, Z. Q.; Wang, W. A phosphatized pseudo-core-shell Fe@Cu-P/C electrocatalyst for efficient hydrazine oxidation reaction. *J. Alloys Compd.* **2019**, *787*, 104–111.

[52] Wen, H.; Gan, L. Y.; Dai, H. B.; Wen, X. P.; Wu, L. S.; Wu, H.; Wang, P. *In situ* grown Ni phosphide nanowire array on Ni foam as a high-performance catalyst for hydrazine electrooxidation. *Appl. Catal. B Environ.* **2019**, *241*, 292–298.

[53] Chen, Y. J.; Ji, S. F.; Wang, Y. G.; Dong, J. C.; Chen, W. X.; Li, Z.; Shen, R. A.; Zheng, L. R.; Zhuang, Z. B.; Wang, D. S. et al. Isolated single iron atoms anchored on N-doped porous carbon as an efficient electrocatalyst for the oxygen reduction reaction. *Angew. Chem., Int. Ed.* **2017**, *56*, 6937–6941.

[54] Yin, W. X.; Li, Z. P.; Zhu, J. K.; Qin, H. Y. Effects of NaOH addition on performance of the direct hydrazine fuel cell. *J. Power Sources* **2008**, *182*, 520–523.

[55] Yamada, K.; Yasuda, K.; Tanaka, H.; Miyazaki, Y.; Kobayashi, T. Effect of anode electrocatalyst for direct hydrazine fuel cell using proton exchange membrane. *J. Power Sources* **2003**, *122*, 132–137.

[56] Kodera, T.; Honda, M.; Kita, H. Electrochemical behaviour of hydrazine on platinum in alkaline solution. *Electrochim. Acta.* **1985**, *30*, 669–675.

[57] Yamada, K.; Asazawa, K.; Yasuda, K.; Ioroi, T.; Tanaka, H.; Miyazaki, Y.; Kobayashi, T. Investigation of PEM type direct hydrazine fuel cell. *J. Power Sources* **2003**, *115*, 236–242.

[58] Agusta, M. K.; Diño, W. A.; David, M.; Nakanishi, H.; Kasai, H. Theoretical study of hydrazine adsorption on Pt(111): Anti or cis? *Surf. Sci.* **2011**, *605*, 1347–1353.

[59] Feng, G.; An, L.; Li, B.; Zuo, Y. X.; Song, J.; Ning, F. H.; Jiang, N.; Cheng, X. P.; Zhang, Y. F.; Xia, D. G. Atomically ordered non-precious Co_3Ta intermetallic nanoparticles as high-performance catalysts for hydrazine electrooxidation. *Nat. Commun.* **2019**, *10*, 4514.

[60] Zhang, J.; Cao, X. Y.; Guo, M.; Wang, H. N.; Saunders, M.; Xiang, Y.; Jiang, S. P.; Lu, S. F. Unique Ni crystalline core/Ni phosphide amorphous shell heterostructured electrocatalyst for hydrazine oxidation reaction of fuel cells. *ACS Appl. Mater. Interfaces* **2019**, *11*, 19048–19055.

[61] Rosca, V.; Koper, M. T. M. Electrocatalytic oxidation of hydrazine

on platinum electrodes in alkaline solutions. *Electrochim. Acta.* **2008**, *53*, 5199–5205.

[62] Yang, J. R.; Li, W. H.; Wang, D. S.; Li, Y. D. Electronic metal–support interaction of single-atom catalysts and applications in electrocatalysis. *Adv. Mater.* **2020**, *32*, 2003300.

[63] Chen, Y. J.; Gao, R.; Ji, S. F.; Li, H. J.; Tang, K.; Jiang, P.; Hu, H. B.; Zhang, Z. D.; Hao, H. G.; Qu, Q. Y. et al. Atomic-level modulation of electronic density at cobalt single-atom sites derived from metal–organic frameworks: Enhanced oxygen reduction performance. *Angew. Chem., Int. Ed.* **2021**, *60*, 3212–3221.

[64] Yang, J. R.; Li, W. H.; Wang, D. S.; Li, Y. D. Single-atom materials: Small structures determine macroproperties. *Small Struct.* **2021**, *2*, 2170006.

[65] Martinez, U.; Rojas-Carbonell, S.; Halevi, B.; Artyushkova, K.; Kiefer, B.; Sakamoto, T.; Asazawa, K.; Tanaka, H.; Datye, A.; Atanassov, P. Ni-La electrocatalysts for direct hydrazine alkaline anion-exchange membrane fuel cells. *J. Electrochem. Soc.* **2014**, *161*, H3106–H3112.

[66] Lu, Z. Y.; Sun, M.; Xu, T. H.; Li, Y. J.; Xu, W. W.; Chang, Z.; Ding, Y.; Sun, X. M.; Jiang, L. Superaerophobic electrodes for direct hydrazine fuel cells. *Adv. Mater.* **2015**, *27*, 2361–2366.